Robust Programmable Photonic Circuits Based on a Floquet-Lieb Topological Waveguide Lattice

Hanfa Song, Tyler J. Zimmerling, *Graduate Student Member, IEEE*, and Vien Van, *Member, IEEE*

***Abstract*—We propose a robust programmable photonic integrated circuit platform based on a 2D Floquet-Lieb topological lattice. Reconfigurable topological photonic lattices typically require creating topologically distinct domains to guide interface modes, which requires a large number of coupling elements to be tuned and severely constraints the realizable circuit configurations. Here by taking advantage of the natural hopping sequence of light in the Floquet-Lieb microring lattice, we show that line defect modes and flat-band resonance modes can be excited by tuning only selective coupling elements, thus enabling efficient light steering and localization in the lattice interior. We show how basic circuit elements such as waveguide bends, splitters, combiners, and resonators, can be formed in the lattice, which can be used to construct general photonic integrated circuits. Compared to conventional topologically-trivial waveguide meshes, our topological photonic lattice requires fewer tuning elements while offering better tolerance to defects and random variations due to topological protection. The proposed topological lattice can thus provide an efficient and robust platform for implementing classical and quantum integrated photonic circuits.**

***Index Terms*—Programmable photonic integrated circuit, robustness, topological photonics.**

I. Introduction

PHOTONIC integrated circuits (PICs) is evolving into a powerful platform for applications in communication, signal processing, artificial intelligence, quantum communication and sensing [1], [2], [3], [4], [5]. While application-specific PICs are well developed, their fixed functionalities and lack of flexibilities make them costly and time consuming to design and manufacture [6], [7]. On the other hand, recent progress in PIC technology has seen increasing interest in the development of programmable photonic processors that can implement various functionalities for rapid prototyping [6], [8], [9], [10], [11], similar to Field Programmable Gate Arrays (FPGAs) in microelectronics. For example, a programmable two-dimensional (2D) network of tunable couplers has been proposed [7], [12], and a seven-hexagonal cell structure has been fabricated in silicon to implement up to 20 functionalities [13]. However, these networks require a large number of couplings to be tuned to form channels for light guiding. In addition, the conventional hexagonal waveguide mesh is sensitive to coupling and phase perturbations due to fabrication imperfections, which becomes more pronounced as the mesh size is increased, thus limiting scalability of the optical FPGA [14], [15].

Topological photonic insulators (TPIs) hosting topologically-protected edge modes in nontrivial band gaps can potentially provide a robust platform for realizing photonic devices that are tolerant to fabrication variations. For example, robust optical delay lines [16] and entangled photon emitters [17] have been demonstrated in silicon TPIs. However, these devices occupy large footprints since they rely on edge modes propagating along the physical boundaries of the lattice while leaving the lattice bulk largely unutilized. Recently, light steering through the lattice interior was demonstrated along an interface between gain and loss domains in the bulk [18]. A reconfigurable topological lattice using coupling and phase tuning has also been reported [19], and beam splitting and routing in a topological photonic crystal by lattice deformation have been demonstrated for far-field steering [20]. A common feature of all these works is that they require topologically distinct regions to be created in the lattice, which requires a large number of unit cells to be modified. As a result, very limited device structures can be created, making these platforms unsuitable for realizing complex reconfigurable PICs.

In this paper we propose a topological photonic lattice that can be used to construct robust programmable PICs. Our topological lattice is a square waveguide mesh, which can also be regarded as a 2D microring lattice with the couplings designed to emulate an anomalous Floquet-Lieb insulator (AFLI) with all flat bands. We have recently experimentally demonstrated non-trivial edge mode propagation in an AFLI lattice fabricated in silicon-on-insulator (SOI) [21]. Here we show that by exploiting the natural hopping sequence of light in the ring lattice, we can form a new type of line defect modes and flat-band resonance modes by selectively tuning only certain coupling elements. These defect modes provide efficient mechanisms to steer and localize light in the lattice interior without having to create entire topological distinct domains, as required for interface mode guidance in previous reconfigurable TPI lattices. We also investigate the performance of the AFLI in the presence of realistic levels of fabrication-induced variations, and provide a method for estimating coupling disorder from experimental measurement of the edge mode transmission spectrum of the lattice. Compared to conventional, topologically trivial waveguide meshes [9], our topological lattice requires fewer tuning elements to realize the same PIC while offering the advantage of robustness to

Manuscript received 13 June 2023; revised 29 July 2023; accepted 7 August 2023. Date of publication 10 August 2023; date of current version 18 August 2023. This work was supported by the Natural Sciences and Engineering Research Council of Canada. *(Corresponding author: Hanfa Song.)*

The authors are with the Department of Electrical and Computer Engineering, University of Alberta, Edmonton T6G 2V4, Canada (e-mail: hanfa@ualberta.ca).

Digital Object Identifier 10.1109/JPHOT.2023.3304188

This work is licensed under a Creative Commons Attribution 4.0 License. For more information, see https://creativecommons.org/licenses/by/4.0/

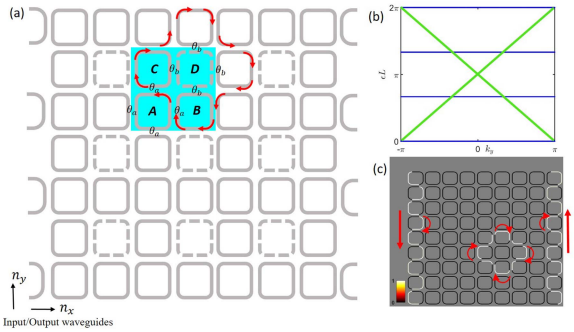

Fig. 1. (a) Schematic diagram of the programmable AFLI lattice. Each unit cell consists of 4 microrings A, B, C and D with coupling angles θ_a and θ_b. Light hopping sequence is indicated by the red arrows. (b) Projected band diagram of an AFLI lattice (for $\theta_a = \pi/2, \theta_b = \pi$) with $N_x = 10$ unit cells in the x-direction and infinite extent along y. (c) Intensity distributions of the edge modes and flat-band bulk mode at quasienergy $\epsilon = 0$.

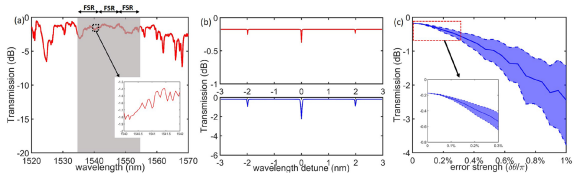

Fig. 2. (a) Measured edge mode transmission spectrum of a 10×10 AFLI lattice fabricated on SOI. Inset shows the zoomed-in ripples of the spectrum due to measurement uncertainty. (b) Simulated edge mode transmission spectra over one FSR with coupling disorder strength of $\epsilon_\theta = 0.2\%\pi$ (upper panel) and $\epsilon_\theta = 1\%\pi$ (lower panel). (c) Variation of edge mode transmission at the flat-band mode quasienergy $\epsilon = 0$ (zero wavelength detune) against coupling disorder strength. Solid line indicates the transmission mean and shaded area indicates $\pm 1\sigma$ (standard deviation) range.

fabrication-induced disorder due to the topological protection property of the AFLI. We demonstrate how to form basic circuit elements in the AFLI such as 90° bends, splitters/combiners, and resonators that are used to construct most photonic circuits, and provide an example implementation of a Mach-Zehnder interferometer (MZI) circuit with one arm coupled to a ring resonator. The proposed AFLI lattice can thus provide an efficient and robust platform for implementing programmable classical and quantum photonic circuits.

II. Programmable Topological Photonic Lattice

Fig. 1(a) shows a schematic of the programmable topological waveguide mesh in the form of a square microring lattice, with each unit cell composed of four identical microrings labeled A, B, C and D. Each microring is assumed to support only a clockwise or counterclockwise propagating mode, with negligible scattering into the reverse direction. We define the coupling angle between microring A and its neighbors as θ_a, and between microring D and its neighbors as θ_b, such that the fraction of power transfer between two neighbor rings is given by $\sin^2 \theta_{(a,b)}$. Nontrivial topological behavior of the lattice can be obtained for certain values of θ_a and θ_b [22]. For our topological programmable lattice, we want to maximize the nontrivial band gaps while minimizing the bulk bands to provide the widest edge mode transmission bandwidth possible. This can be achieved by setting $\theta_a = \pi/2$ and $\theta_b = \pi$, which correspond to 100% power coupling between microring A and its neighbors, and no coupling between microring D and its neighbors. For this choice of coupling angles the lattice behaves as an anomalous Floquet Lieb insulator (AFLI) with three flat bands at quasienergies $\epsilon = 0, \pm 2\pi/3\ L$ in each microring FSR, where L is the microring circumference [21]. Fig. 1(b) shows the projected band diagram over one FSR of an AFLI lattice with $N_x = 10$ unit cells in the x direction and infinite extent in y (details of band diagram calculation can be found in the Supplemental Material of [23]). We observe two linearly-dispersive edge modes spanning the full FSR, intersecting the three flat bands at discrete points of degeneracy. The intensity distributions of the edge modes are shown in Fig. 1(c), indicating light propagating along the left and right lattice boundaries. To visualize the flat-band modes, we also computed the intensity distribution of the eigenmode at quasienergy $\epsilon = 0$ in a 5×5 unit cell lattice. The result is also displayed in Fig. 1(c), showing light localized in a loop pattern which corresponds to the hopping sequence of the Floquet microring lattice (shown by red arrows in Fig. 1(a)). In general, these flat-band modes have a two-fold degeneracy with opposite chirality, corresponding to the clockwise and counterclockwise directions of propagation around the loop, which can be independently excited. The strong spatial localization of the flat-band modes suggests that they can be exploited to realize high-Q resonators anywhere in the lattice, as shown in Section II-B below.

A striking feature of our AFLI lattice is that the edge modes can coexist with the flat-band modes at the degenerate frequencies and these modes are orthogonal so they do not couple to each other [21]. As a result, we can obtain a broad and continuous spectrum of edge modes spanning multiple microring FSRs without exciting the flat-band resonances, which is necessary for broadband applications of the programmable lattice. We have experimentally verified the existence of this broad edge mode continuum in AFLI microring lattices fabricated on SOI using the AMF foundry [21]. A sample measured TE transmission spectrum of an edge mode propagating along the bottom lattice boundary is shown in Fig. 2(a). The fabricated lattice has 10×10 unit cells, with each ring having circumference $L = 103.4\,\mu$m and FSR of 6 nm (see Appendix A for detailed lattice design). A wide region of high and flat edge mode transmission can be seen between 1535 nm and 1553 nm in the measured spectrum, corresponding to 3 microring FSRs. Direct evidence of an edge mode propagating along the lattice boundary in this wavelength range could also be obtained from Near Infrared imaging of the scattered light from the lattice [21]. The absence of sharp dips in this spectral range indicates that the flat-band resonance modes were not excited. However, if there is sufficiently large disorder in the coupling angles in the lattice, such as due to fabrication variations, the orthogonality between the edge modes and flat-band modes can be destroyed, causing transmission dips to appear in the edge mode spectrum (the lattice is immune to disorder in microring phase detunes, as illustrated in Fig. 4(c)). Fig. 2(b) shows the simulated edge mode transmission spectra

of the AFLI lattice in the presence of uniformly-distributed coupling error $|\delta\theta_i| \leq \epsilon_\theta$, where $\delta\theta_i$ is the deviation of the coupling angle θ_i from the nominal value and ϵ_θ is the error bound (see Appendix B for simulation method). The upper panel is for disorder level $\epsilon_\theta = 0.2\%\pi$ while the lower panel is for $\epsilon_\theta = 1\%\pi$. A nominal propagation loss of 3 dB/cm was also assumed in the microring waveguides, which accounts for material absorption, surface roughness scattering and bending loss. We observe transmission dips appearing at the flat-band frequencies, which increase with increasing disorder level. The variation of the edge mode transmission at a flat-band frequency as a function of the coupling error strength ϵ_θ is plotted in Fig. 2(c). We note that coupling disorder also causes similar dips to appear in the transmission spectra of conventional waveguide lattices and this is a common issue with recirculating meshes [9]. The level of fabrication-induced disorder that can be tolerated by these waveguide lattices is determined by the magnitudes of the dips that can be tolerated in broadband PIC applications.

It is possible to estimate the level of coupling disorder in the fabricated AFLI lattice from the size of the transmission dips. Given that the ripples in the measured edge mode spectrum are about 0.2 dB, we estimate a maximum coupling disorder of $\epsilon_\theta \sim \pm 0.2\%\pi$ in the lattice. If we assume that this coupling angle variation is due to variation in the microring waveguide width w, which is accompanied by a corresponding change in the coupling gap, we can estimate the width variation to be $\delta w \sim w(\epsilon_\theta/\theta_a) \sim \pm 2$ nm. This estimate is reasonable for state-of-the-art silicon photonics fabrication technology [24].

A. *Line Defect Modes in AFLI Microring Lattice*

The main drawback of steering light by the edge modes is that they can only guide light along the lattice boundaries, leaving the large area of the bulk unused. While there have been proposals to guide edge modes through the bulk by creating domain walls between topologically distinct regions in the lattice [18], [19], [20], these approaches are inefficient since they require altering every unit cell in the new topological region. Here we show how a line defect mode can be created in the AFLI for light guidance through the lattice interior by tuning only the coupling elements along the line mode. In particular, to create a line defect mode propagating along the y-direction through the lattice interior, we simply turn off the coupling between rings A and B (i.e., tune θ_a to π) in each unit cell along the line mode, as indicated by the red crosses in Fig. 3(a). Effectively, the lattice is "cut" into two separate domains, so that an edge mode can be supported on either side of this interior domain wall. Fig. 3(c) shows the projected band diagram of an AFLI lattice with $N_x = 5$ unit cells and infinite extent along y with the $A - B$ couplings of the unit cells at position $n_x = 3$ turned off. In addition to the two edge modes at the left and right boundaries of the lattice (green lines), we observe two additional modes (orange and black lines) existing in each band gap. The intensity distributions of these modes are shown in Fig. 3(a) and (b), confirming that they are edge modes propagating along the interior domain wall in opposite directions. For light steering applications, it is preferable to employ the forward-travelling line mode in Fig. 3(a) since it

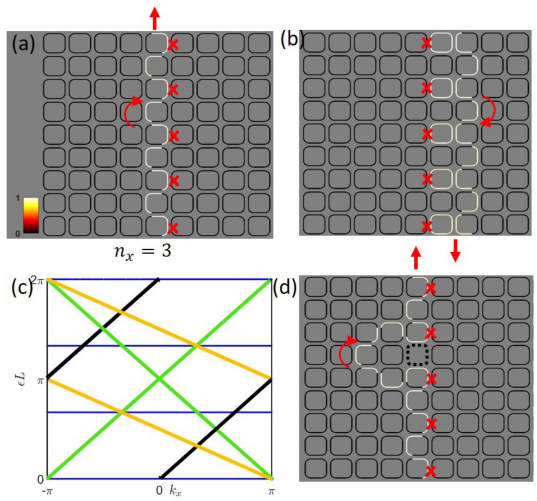

Fig. 3. (a) and (b) Creation of line defect modes propagating along the positive and negative y-directions, respectively, through the AFLI lattice interior by turning off the $A - B$ couplings in unit cells at $n_x = 3$ (indicated by red crosses). The simulated intensity distributions of the line modes are also shown. (c) Projected band diagram of a lattice with $N_x = 5$ unit cells and infinite extent along y, with the $A - B$ coupling angle of unit cells at $n_x = 3$ tuned to π. Green lines correspond to edge modes along the left and right lattice boundaries; black and orange lines are the forward and backward propagating line defect modes, respectively. (d) Intensity distribution of a line mode going around a defect created by removal of a microring C (dashed black square) in its path.

is more localized than the backward mode. In general, we can create light channels along the x or y direction by turning off the $A - B$ or $A - C$ coupling, respectively, in each unit cell through which the line mode propagates. Note that we need to tune only one coupling per unit cell along the line defect mode, instead of altering an entire region of the lattice to create an interface between topologically distinct domains. Fig. 3(d) demonstrates the topological protection of the line mode by showing that it goes around a defect caused by the removal of a site microring in its path. It should be noted that unlike the external lattice boundaries, the interior domain wall created by turning off the couplings along the interface is a "soft" boundary since light can leak to the other side in the presence of coupling disorder. We will investigate the robustness of the line defect mode to random disorder below.

It is also of interest to compare the light steering performance in our topological lattice to conventional programmable 2D waveguide meshes that have previously been proposed [9], [12]. We focus on two types of networks, "All Bar" (AB) and "All Cross" (AC), shown in Fig. 4(a) and (b), which are similar to the hexagonal meshes proposed in [9] except that here we use a square mesh configuration for direct comparison with our topological lattice. The AB lattice has all coupling junctions in the bar state by default (coupling angles $\theta_a = \theta_b = \pi$) while the AC lattice has all coupling junctions in the cross state by default ($\theta_a = \theta_b = \pi/2$). Both lattices are topologically trivial. To create light channel in each mesh, selective coupling junctions are turned on or off as indicated by the crosses in Fig. 4(a) and (b) for a line mode propagating along the y direction. We observe that the line mode patterns are the same as in the topological lattice (Fig. 3(a)) but for the same waveguide length,

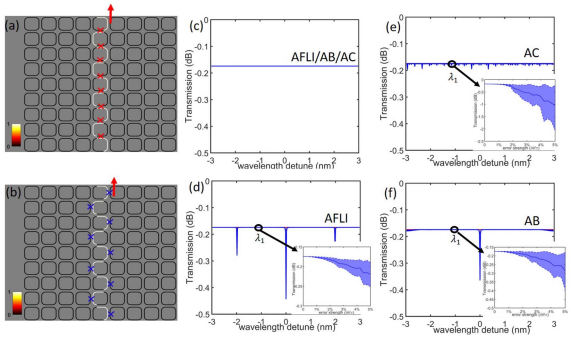

Fig. 4. Intensity distributions of line modes in (a) "All Bar" (AB) lattice and (b) "All Cross" (AC) lattice. The red (blue) crosses indicate the coupling junctions being turned on (off). (c) Transmission of line modes over 1 FSR in the AFLI, AB and AC lattices in the presence of random variations in the microring roundtrip phases ($|\delta\phi_i| < 2\pi$). (d)–(f) Transmission of line modes in the (d) AFLI, (e) AB and (f) AC lattices in the presence of random variations in the coupling angles ($|\delta\theta_i| < 0.2\%\pi$). The insets show the variation in the transmission at wavelength λ_1 in the middle of a band gap as a function of the coupling error strength.

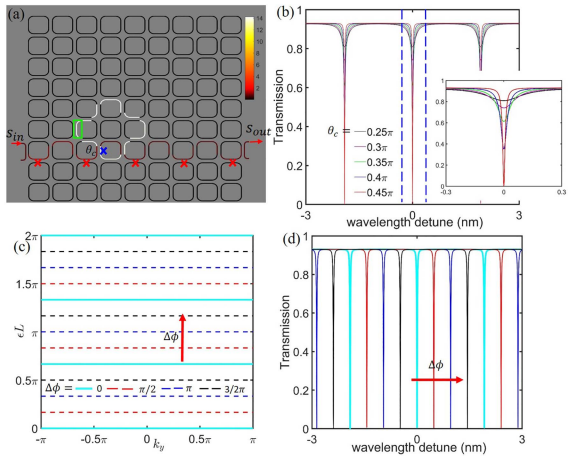

Fig. 5. (a) Intensity distribution of a flat-band resonance mode at zero quasienergy coupled to an edge mode. The resonance is excited by tuning coupling angle θ_c (blue cross) to 0.35π. (b) Power transmission spectra of the flat-band mode resonator for various values of coupling angle θ_c. (c) Projected band diagrams of flat band-modes for various phase detune values $\Delta\phi$ applied to the microring segment marked by the green box in (a). (d) Resonance spectra corresponding to applied phase detune values in (c).

both the AB and AC meshes require twice as many couplers to be tuned compared to the AFLI lattice. Thus in general we expect the topological lattice to require fewer coupler tunings as the conventional meshes to realize the same PIC.

To compare the robustness of the three lattices to random disorder, we performed Monte-Carlo simulations of light propagation along a line mode through each lattice with 10×10 unit cells subject to uniformly-distributed coupling and microring roundtrip phase errors (see Appendix B for simulation method). A nominal propagation loss of 3 dB/cm was assumed in the microring waveguides. For all three lattices, we found that the power transmission of the line mode is immune to microring phase errors, as shown in Fig. 4(c) for uniformly-distributed phase errors in the range $|\delta\phi_i| < 2\pi$. This is expected since in the absence of coupling errors, light in each ring does not recirculate so the rings do not act as resonators. As a result, the power transmission of the line mode does not depend on the ring roundtrip phases. For the case of coupling disorder, we assumed the coupling error bound to be $|\delta\theta_i| < 0.2\%\pi$ as estimated from the measured edge mode transmission spectrum in Fig. 2(a). The simulated line mode transmission spectra for the three lattices are shown in Fig. 4(d)–(f). We observe spurious dips appearing in all three transmission spectra, which are caused by the interference of recirculating light or excitation of resonant bulk modes. However, the dips remain less than 0.25 dB, which is tolerable for most applications and can be reduced with better fabrication control. For the AFLI lattice, the transmission of the line mode shows remarkable robustness to disorder at frequencies in the topological band gaps. The insets of Fig. 4(d)–(f) show the variations in the transmission of the line modes at wavelength λ_1 in the middle of a band gap as a function of the coupling disorder strength. We observe that the line mode in the AFLI lattice exhibits less variation than both the AB and AC meshes, with the AC lattice performing the worst. Thus the AFLI lattice is more robust than the conventional meshes at frequencies in the topological band gaps, although it suffers from larger transmission dips at the flat-band frequencies.

B. Flat-Band Mode Resonance

As shown in Fig. 1(b), a distinctive feature of the AFLI lattice is that it hosts three flat bands within each FSR. These flat-band modes form localized spatial loop patterns in the bulk, which can be exploited to form compact, high-Q resonators anywhere in the lattice interior by tuning only one coupling junction. In particular, these resonant modes can be excited and coupled to an edge mode or a line defect mode by tuning the coupler shared by the two modes to break the mode orthogonality. As an example, Fig. 5(a) shows a flat-band resonance excited by an edge mode by tuning the $A - B$ coupling angle (θ_c) indicated by the blue cross. This loop is excited whenever the frequency of the edge mode coincides with the quasienergy of a flat-band mode $(0, \pm 2\pi/3\ L)$. As a result, the spectral response of the transmitted light at the output port has three resonance dips over each FSR, as shown in Fig. 5(b). Effectively the resonator behaves as an all-pass ring filter. The Q factor of the resonator can be varied by tuning the coupling angle θ_c, as demonstrated in the inset of Fig. 5(b). Specifically, the Q factor decreases for larger deviation of the coupling angle θ_c from the initial value $\theta_a = \pi/2$, indicating stronger coupling between the edge mode and the flat-band mode.

It is also possible to vary the resonance frequencies of the flat-band modes by introducing a phase detune in the resonant loop. For example, for the resonator in Fig. 5(a), we can tune its resonance frequency by varying the phase of a microring waveguide segment in the loop, as indicated by the green box. The phase detune $\Delta\phi$ can be achieved, for example, using the thermo-optic effect by heating up the indicated waveguide segment. Fig. 5(c) shows the projected band diagrams of a 5×5 unit cell lattice for several values of phase detune $\Delta\phi$ applied to the microring segment. We observe that the effect of the phase detune is simply to shift the quasienergies of the flat-band modes while maintaining their flatness. Fig. 5(d) shows the

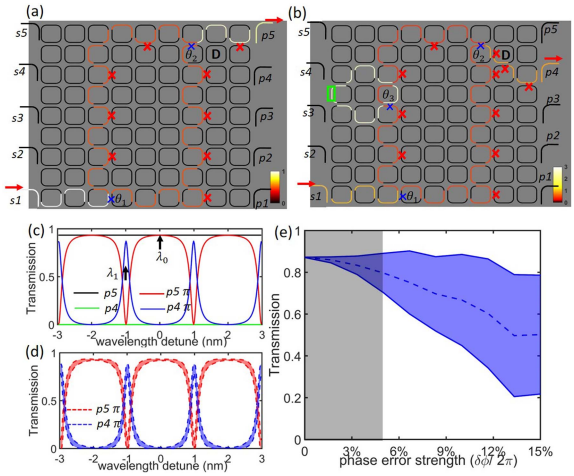

Fig. 6. Implementation of PIC in the AFLI circuit: (a) an MZI and (b) an MZI with left arm coupled to a flat-band mode resonance. Red crosses indicate coupling junctions to be turned off to form the circuits. The simulated light intensity distribution in each circuit is also shown. (c) Power transmission spectra at output ports p_4 and p_5 of the MZI (black and green lines) and the ring-coupled MZI (red and blue lines) with $\theta_3 = \pi/4$ and phase detune $\Delta\phi = \pi$. (d) Transmission spectra of the ring-coupled MZI in the presence of $0.2\%\pi$ coupling disorder and $3\%\pi$ phase detune disorder. (e) Plot of the peak transmission variation (1σ) vs. phase detune disorder level.

transmission spectrum obtained for each phase detune. The resonance spectrum is increasingly red shifted for larger phase detune value while its shape remains unaffected. The flat-band modes thus provide an efficient mechanism for forming resonators with tunable wavelength and Q factor anywhere in the AFLI lattice by varying only one coupling and one phase shift element. We note that a similar type of resonance called Floquet Defect Mode Resonance (FDMR) has been experimentally demonstrated in a general 2D Floquet microring lattice [25], except that the bulk bands of those lattices were not flat. The main advantage of the AFLI proposed here is that all the bulk bands always remain flat in the presence of frequency detunes. As a result, the resonance spectrum of the flat-band mode maintains its shape and linewidth as it is tuned across the band gap, which is not the case for the FDMR.

III. Example of a Topological Programmable Circuit

As an application example of the programmable topological platform, we demonstrate a PIC consisting of an MZI with one arm coupled to a resonator, which may be used as a tunable filter. To implement the MZI, we realize a 3 dB beam splitter by tuning coupling angle θ_1 indicated in Fig. 6(a) to $\pi/4$ to split the input signal from port s_1 into two equal parts propagating at 90° to each other. The two beams are then steered toward each other by two 90° bends, then combined through a beam combiner by tuning coupling angle θ_2 to $\pi/4$. The coupling junctions that need to be turned off to form the MZI are marked by the red crosses in Fig. 6(a). Fig. 6(c) shows the transmission spectra over one microring FSR at the two output ports p_4 and p_5 of the MZI (black and green lines). For this balanced MZI, the transmission spectra have negligible frequency dependence, with all input power transmitted to output port p_5. The simulated intensity distribution of light propagating through the MZI at a microring resonance wavelength λ_0 is also shown in Fig. 6(a).

To excite a flat-band resonance mode coupled to the left arm of the MZI, we vary the coupling angle θ_3 shown in Fig. 6(b) to achieve the desired Q-factor. We also tune the resonance wavelength to the middle of the band gap by applying a phase detune $\Delta\phi = \pi$ to a microring segment in the resonance loop indicated by the green box in the figure. The transmission spectra at the two MZI output ports for $\theta_3 = \pi/4$ are shown by the red and blue traces in Fig. 6(c). Over one microring FSR, we observe three resonance peaks appearing at output port p_4 corresponding to a flat-band resonance in each band gap. The light intensity distribution in the circuit at a peak transmission wavelength λ_1 is also shown in Fig. 6(b).

We also investigated the robustness of the PIC by performing Monte-Carlo simulations of the lattice in the presence of random disorder. We assumed a fixed coupling disorder of $|\delta\theta_i| < 0.2\%\pi$ obtained from measurement and investigated the effect of random microring phase detune $\delta\phi_j$. Fig. 6(d) shows the variations in the transmission spectra for phase detune disorder $|\delta\phi_j| < 6\%\pi$ (or 3% of microring FSR). It can be seen that the main effects of the disorder are to cause a decrease in the peak transmission and a slight broadening of the resonance spectra. In Fig. 6(e) we plotted the variation in the peak transmission (at wavelength λ_1) as a function of the microring phase disorder strength, with the coupling disorder fixed at $0.2\%\pi$. The plot shows that to keep the peak transmission variation to less than $\pm 5\%$ of the nominal value, the lattice can tolerate microring phase disorder up to $\pm 10\%\pi$ (or 5% of microring FSR), which is achievable with current SOI fabrication technology [24].

IV. Conclusion

We proposed a robust and efficient programmable PIC platform based on a 2D topological photonic lattice. By taking advantage of the natural hopping sequence of the AFLI lattice, we showed that line defect modes and flat-band resonance modes can be efficiently excited for light steering by tuning only certain coupling elements, without having to create entirely new topological domains. Compared to conventional waveguide meshes, the topological lattice requires fewer coupling elements to be tuned while offering better tolerance to random fabrication-induced variations. While we focused on the square lattice in this work, hexagonal topological ring lattices [20] can also be used for robust light steering and localization by creating similar line defect modes and flat-band modes.

In the practical implementation of the programmable topological lattice on SOI, the coupler and phase tunings can be achieved using a phase change material (PCM) such as GST or GSST [26], [27]. By depositing a layer of PCM on top of the lattice, the effective index of the SOI waveguides can be tuned by altering the phase of the PCM between amorphous to crystalline using a pulsed laser [28]. The change in the effective index can be used to tune the coupling between adjacent microrings, for example, by using a three-waveguide directional coupler with a PCM layer deposited on the middle waveguide as demonstrated in [26]. The proposed topological waveguide mesh can provide

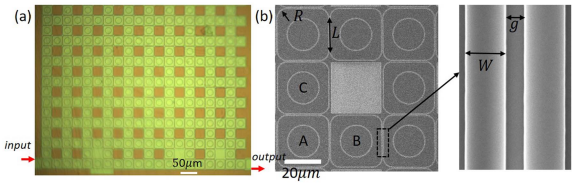

Fig. 7. (a) Optical image of an AFLI lattice with 10×10 unit cells fabricated on SOI. (b) Scanning electron microscopy image showing a close-up view of a unit cell.

an efficient and robust platform for implementing programmable classical and quantum photonic circuits.

Appendix A
Design and Fabrication of AFLI Lattices on SOI

We fabricated AFLI lattices on SOI using the AMF foundry service [29]. The lattices had 10×10 unit cells, each unit cell consisting of 3 squared-shaped ring resonators A, B, C, with ring D omitted to emulate the zero coupling condition ($\theta_b = 0$). Each square-shaped resonator has straight side length $L = 18\,\mu$m and rounded corners with $R = 5\,\mu$m radius, as shown in Fig. 7(b). The microring rib waveguides were designed for TE polarization operation, with $W = 500$ nm core width, 130 nm rib height, and 90 nm slab thickness with SiO_2 overcladding. The coupling gaps between ring A and its neighbors (B and C) were $g = 250$ nm to achieve 100% coupling ($\theta_a = \pi/2$) around 1550 nm wavelength. An optical image of the fabricated lattice is shown in Fig. 7(a), with zoomed-in SEM image of a unit cell in Fig. 7(b). To excite an edge mode along the bottom boundary of the lattice, an input waveguide is coupled to the ring at the lower-left corner of the lattice, as shown in Fig. 7(a). TE-polarized light from a tunable laser is coupled to the input waveguide using a lensed fiber. An output waveguide is coupled to the ring at the lower-right corner to measure the power transmission of the edge mode. The transmitted power in the output waveguide was coupled to a lensed fiber and measured with an InGaAs photodetector.

Appendix B
Method for Simulating Power Transmission and Field Distribution in AFLI Lattice

We used the power coupling method for 2D coupled ring resonators [30] to simulate the field distribution in the AFLI lattice. We consider a finite network consisting of $N \times N$ unit cells with an input waveguide coupled to microring A of the $(n_c, 1)$ unit cell at the bottom and an output waveguide coupled to microring C of the (n_c, N) unit cell at the top of the network, as shown in Fig. 8. We number the unit cells as (m, n), $(m, n = 1 \ldots N)$, with cell (1,1) at the bottom left corner and cell (N, N) at the top right corner. For unit cell (m, n) in the lattice, we denote the fields at position z in microring waveguides A, B, C and D as $[\psi^A_{m,n}(z), \psi^B_{m,n}(z), \psi^C_{m,n}(z), \psi^D_{m,n}(z)]^{\mathrm{T}} = [a_k(z), a_{k+1}(z), a_{k+2}(z), a_{k+3}(z)]^{\mathrm{T}}$, where $k(m, n) = 4[(n-1)N + m - 1] + 1$. Letting $\mathbf{a}(0) = [a_1(0), a_2(0), \ldots, a_{4N^2}(0)]^{\mathrm{T}}$ be the vector containing the fields in all the microrings at the initial position $z = 0$ (indicated by the red bars in Fig. 8), the fields

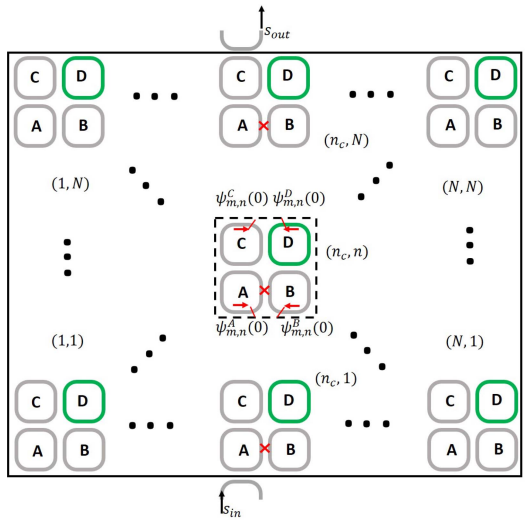

Fig. 8. Schematic of a AFLI microring lattice with $N \times N$ unit cells. The small red bars on each microring indicate the initial position $z = 0$ for light propagation around the microring. To excite a line defect mode along $n_x = n_c$ column, an input field s_{in} is applied to an input waveguide coupled to microring A of cell $(n_c, 1)$ at the bottom. The transmitted light s_{out} is detected through an output waveguide coupled to microring C of cell (n_c, N) at the top of the lattice.

after propagating one roundtrip are given by $\mathbf{a}(L) = \mathbf{M}\mathbf{a}(0)$, where

$$\mathbf{M} = \mathbf{M}_4\mathbf{P}^{-1/4}\mathbf{M}_3\mathbf{P}^{-1/4}\mathbf{M}_2\mathbf{P}^{-1/4}\mathbf{M}_1\mathbf{P}^{-1/4} \tag{1}$$

with $\mathbf{M}_j, j \in \{1, 2, 3, 4\}$ being the coupling matrix for step j and $\mathbf{P} = e^{-\alpha L/2}\mathrm{diag}[e^{i\phi_1}, \ldots, e^{i\phi_{4N^2}}]$ the propagation matrix, where ϕ_k is the roundtrip phase of microring k and α the waveguide loss coefficient. The coupling matrices $\mathbf{M}_j$ are constructed as follows. Starting with $\mathbf{M}_j = \mathbf{I}$ being a $4N^2 \times 4N^2$ identity matrix, if there is coupling between microring waveguides k and l in step j, then $\mathbf{M}_j(k, k) = \mathbf{M}_j(l, l) = \cos\theta$ and $\mathbf{M}_j(k, l) = \mathbf{M}_j(l, k) = i\sin\theta$, where $\theta \in \{\theta_a, \theta_b\}$ is the coupling angle of the AFI lattice. Additionally, to realize the line defect mode along column $n_x = n_c$, the coupling between microrings A and B are turned off for each unit cell along the very column as indicated by the red crosses in Fig. 8.

For a field s_{in} applied to the input port, the fields $\mathbf{a}(0)$ in the microrings satisfy the equation [30]

$$(\mathbf{I} - \mathbf{L}\mathbf{M})\mathbf{a}(0) = \mathbf{s} \tag{2}$$

where $\mathbf{s} = [0, \ldots, 0, i\kappa_o s_{\text{in}}, 0, \ldots, 0]^{\mathrm{T}}$ and $\mathbf{L}$ is a diagonal matrix with diagonal elements

$$\mathbf{L}(k, k) = \begin{cases} \tau_0, k \in \{k(n_c, 1), k(n_c, N) + 2\} \\ 1, \text{ otherwise} \end{cases} \tag{3}$$

Here $\kappa_o = \sin\theta$ and $\tau_o = \cos\theta$ are the coupling and transmission coefficients, respectively, of the coupling junction between the input/output waveguides and the microring. Solving the above equation for $\mathbf{a}$ we obtain the power transmission at the output port of the lattice as

$$T_{\text{out}} = |s_{\text{out}}/s_{\text{in}}|^2 = \kappa_o^2|\psi^C_{n_c,N}(0)|^2/\tau_o^2 \tag{4}$$

To simulate the transmission of the AFI network in the presence of randomly distributed microring roundtrip phases, we set the roundtrip phase in microring k to be $\phi_k = \phi_k^{\text{nom}} + \delta\phi_k$, where ϕ_k^{nom} is the nominal roundtrip phase without perturbation and $\delta\phi_k$ is a random phase error under uniform distribution. Similarly, for random variations in the coupling angles, we add a random term $\delta\theta_k$ to the nominal value of each coupling angle to obtain $\theta_l = \theta_l^{\text{nom}} + \delta\theta_l$. The transmission of the lattice is then calculated with the perturbed couplings and round-trip phases.

ACKNOWLEDGMENT

Hanfa Song would like to thank Fan Yang from Aarhus University and Shunyu Yao from Stanford University for their fruitful suggestions on this paper. Hanfa Song would like to thank Juejun Hu from MIT for his discussions on phase change materials.

REFERENCES

[1] M. Notomi, K. Nozaki, A. Shinya, S. Matsuo, and E. Kuramochi, "Toward fj/bit optical communication in a chip," *Opt. Commun.*, vol. 314, pp. 3–17, 2014.

[2] B. Corcoran et al., "Optical signal processing on a silicon chip at 640GB/s using slow-light," *Opt. Exp.*, vol. 18, no. 8, pp. 7770–7781, 2010.

[3] Y. Li et al., "On-chip photonic microsystem for optical signal processing based on silicon and silicon nitride platforms," *Adv. Opt. Technol.*, vol. 7, no. 1–2, pp. 81–101, 2018.

[4] F. Dell'Olio and V. M. Passaro, "Optical sensing by optimized silicon slot waveguides," *Opt. Exp.*, vol. 15, no. 8, pp. 4977–4993, 2007.

[5] D. Piccinotti, K. F. MacDonald, S. A. Gregory, I. Youngs, and N. I. Zheludev, "Artificial intelligence for photonics and photonic materials," *Rep. Prog. Phys.*, vol. 84, no. 1, 2020, Art. no. 012401.

[6] W. Bogaerts et al., "Programmable photonic circuits," *Nature*, vol. 586, no. 7828, pp. 207–216, 2020.

[7] D. Pérez, I. Gasulla, J. Capmany, and R. A. Soref, "Reconfigurable lattice mesh designs for programmable photonic processors," *Opt. Exp.*, vol. 24, no. 11, pp. 12093–12106, 2016.

[8] M. Milanizadeh, D. Aguiar, A. Melloni, and F. Morichetti, "Canceling thermal cross-talk effects in photonic integrated circuits," *J. Lightw. Technol.*, vol. 37, no. 4, pp. 1325–1332, Feb. 2019.

[9] I. Zand and W. Bogaerts, "Effects of coupling and phase imperfections in programmable photonic hexagonal waveguide meshes," *Photon. Res.*, vol. 8, no. 2, pp. 211–218, 2020.

[10] S. Bandyopadhyay, R. Hamerly, and D. Englund, "Hardware error correction for programmable photonics," *Optica*, vol. 8, no. 10, pp. 1247–1255, 2021.

[11] N. C. Harris et al., "Linear programmable nanophotonic processors," *Optica*, vol. 5, no. 12, pp. 1623–1631, 2018.

[12] L. Zhuang, C. G. Roeloffzen, M. Hoekman, K.-J. Boller, and A. J. Lowery, "Programmable photonic signal processor chip for radiofrequency applications," *Optica*, vol. 2, no. 10, pp. 854–859, 2015.

[13] D. Pérez et al., "Multipurpose silicon photonics signal processor core," *Nature Commun.*, vol. 8, no. 1, pp. 1–9, 2017.

[14] S. Pai, B. Bartlett, O. Solgaard, and D. A. Miller, "Matrix optimization on universal unitary photonic devices," *Phys. Rev. Appl.*, vol. 11, no. 6, 2019, Art. no. 064044.

[15] D. Pérez and J. Capmany, "Scalable analysis for arbitrary photonic integrated waveguide meshes," *Optica*, vol. 6, no. 1, pp. 19–27, 2019.

[16] M. Hafezi, E. A. Demler, M. D. Lukin, and J. M. Taylor, "Robust optical delay lines with topological protection," *Nature Phys.*, vol. 7, no. 11, pp. 907–912, 2011.

[17] T. Dai et al., "Topologically protected quantum entanglement emitters," *Nature Photon.*, vol. 16, no. 3, pp. 248–257, 2022.

[18] H. Zhao, X. Qiao, T. Wu, B. Midya, S. Longhi, and L. Feng, "Non-hermitian topological light steering," *Science*, vol. 365, no. 6458, pp. 1163–1166, 2019.

[19] D. Leykam, S. Mittal, M. Hafezi, and Y. D. Chong, "Reconfigurable topological phases in next-nearest-neighbor coupled resonator lattices," *Phys. Rev. Lett.*, vol. 121, no. 2, 2018, Art. no. 023901.

[20] T. Wu, Y. Li, X. Feng, S. Wu, Z. Gao, and L. Feng, "Topological photonic lattice for uniform beam splitting, robust routing, and sensitive far-field steering," *Nano Lett.*, vol. 23, pp. 3866–3871, 2023.

[21] H. Song, T. Zimmerling, B. Leng, and V. Van, "Ultrawide edge state supercontinuum in a floquet-lieb topological photonic insulator," 2023, *arXiv:2305.05707*.

[22] S. Afzal and V. Van, "Topological phases and the bulk-edge correspondence in 2D photonic microring resonator lattices," *Opt. Exp.*, vol. 26, no. 11, pp. 14567–14577, 2018.

[23] T. J. Zimmerling, S. Afzal, and V. Van, "Broadband resonance-enhanced frequency generation by four-wave mixing in a silicon floquet topological photonic insulator," *APL Photon.*, vol. 7, no. 5, 2022, Art. no. 056104.

[24] Y. Xing, J. Dong, U. Khan, and W. Bogaerts, "Capturing the effects of spatial process variations in silicon photonic circuits," *ACS Photon.*, vol. 10, pp. 928–944, 2022.

[25] S. Afzal and V. Van, "Trapping light in a floquet topological photonic insulator by floquet defect mode resonance," *APL Photon.*, vol. 6, no. 11, 2021, Art. no. 116101.

[26] P. Xu, J. Zheng, J. K. Doylend, and A. Majumdar, "Low-loss and broadband nonvolatile phase-change directional coupler switches," *Acs Photon.*, vol. 6, no. 2, pp. 553–557, 2019.

[27] Q. Zhang, Y. Zhang, J. Li, R. Soref, T. Gu, and J. Hu, "Broadband nonvolatile photonic switching based on optical phase change materials: Beyond the classical figure-of-merit," *Opt. Lett.*, vol. 43, no. 1, pp. 94–97, 2018.

[28] P. Li et al., "Reversible optical switching of highly confined phonon–polaritons with an ultrathin phase-change material," *Nature Mater.*, vol. 15, no. 8, pp. 870–875, 2016.

[29] [Online]. Available: https://www.advmf.com/

[30] V. Van, *Optical Microring Resonators: Theory, Techniques, and Applications*. Boca Raton, FL, USA: CRC Press, 2016.